

Supraglacial lake drainage at a fast-flowing Greenlandic outlet glacier

Thomas R. Chudley^{a,1}, Poul Christoffersen^{a,1}, Samuel H. Doyle^b, Marion Bougamont^a, Charlotte M. Schoonman^a, Bryn Hubbard^b, and Mike R. James^c

^aScott Polar Research Institute, University of Cambridge, Cambridge, UK, CB2 1ER.; ^bCentre for Glaciology, Department of Geography and Earth Sciences, Aberystwyth University, Aberystwyth, UK, SY23 3DB.; ^cLancaster Environment Centre, University of Lancaster, Lancaster, UK, LA1 4YQ.

This manuscript was compiled on October 23, 2019

1 **Supraglacial lake drainage events influence Greenland Ice Sheet dy-**
2 **namics on hourly to interannual timescales. However, direct observa-**
3 **tions are rare and, to date, no *in-situ* studies exist from fast-flowing**
4 **sectors of the ice sheet. Here, we present novel observations of a**
5 **rapid lake drainage event at Store Glacier, West Greenland, in 2018.**
6 **The drainage event transported 4.8×10^6 m³ of meltwater to the**
7 **glacier bed in ~ 5 hours, reducing the lake to a third of its original**
8 **volume. During drainage, the local ice surface rose by 0.55 m and**
9 **surface velocity increased from 2.0 m d⁻¹ to 5.3 m d⁻¹. Dynamic re-**
10 **sponses were greatest ~ 4 km downstream from the lake, which we**
11 **interpret as an area of transient water storage constrained by basal**
12 **topography. Drainage initiated, without any precursory trigger, when**
13 **the lake expanded and reactivated a pre-existing fracture that had**
14 **been responsible for a drainage event one year earlier. Since for-**
15 **mation, this fracture had advected ~ 600 m from the lake's deepest**
16 **point, meaning the lake did not fully drain. Partial drainage events**
17 **have previously been assumed to occur slowly via lake overtopping,**
18 **with a comparatively small dynamic influence. In contrast, our find-**
19 **ings show that partial drainage events can be caused by hydrofract-**
20 **ture, producing new hydrological connections that continue to con-**
21 **centrate the supply of surface meltwater to the bed of the ice sheet**
22 **throughout the melt season. Our findings therefore indicate that the**
23 **quantity and resultant dynamic influence of rapid lake drainages are**
24 **likely being under-estimated.**

Greenland | glaciology | ice sheets | lakes | hydrology

1 **V**ariation in the rate of meltwater input into the subglacial
2 system of the Greenland Ice Sheet forces dynamic re-
3 sponses at a range of scales, from hourly (1–3) to seasonal
4 (4–6) and longer (7, 8). A notable source of meltwater delivery
5 is via rapid supraglacial lake drainages, whereby lakes drain
6 to the bed of a glacier or ice sheet in the space of a few hours.
7 The large volume of water delivered rapidly to the bed during
8 drainage results in hydraulic ice-bed separation, which is ex-
9 pressed at the surface as decimetre-scale ice uplift (2, 9, 10).
10 These evacuations induce short-term ice-flow accelerations via
11 a reduction in basal traction (1, 2, 11), modifying the seasonal
12 efficiency of the subglacial system (5, 12, 13), and opening
13 new surface-to-bed connections (14) that can then continue to
14 deliver meltwater to the bed (15). Since the advent of satellite
15 records in the 1970s, supraglacial lakes have formed in greater
16 numbers, at higher elevations, and at larger sizes in response
17 to warmer summers (16–18). However, the net effect of an
18 increasing meltwater supply on the dynamics of the Greenland
19 ice sheet is the subject of ongoing debate (7, 8, 19–21).

20 Satellite observations show that 28%–45% of all supraglacial
21 lakes in West Greenland drain rapidly (17, 18), although
22 multi-year studies indicate that even lakes that exhibit rapid
23 drainage behaviour do so in fewer than half of years (22,

23). Rapid drainage occurs when water opens a surface-to-
24 bed connection via hydraulic fracture (1–3). However, the
25 exact timing of hydrofracture is seemingly stochastic, with
26 studies failing to support the hypothesis that the drainage of
27 lakes can be explained by any critical thresholds relating to
28 lake hydrology (depth, volume, or morphology), glaciological
29 setting (hypsometry, velocity, or strain) or meteorological
30 conditions (17, 24). Lakes often drain in clusters (17) because
31 the transfer of water to the base of the ice sheet when one lake
32 drains increases the tensile stresses near other lakes, triggering
33 further hydrofractures (25). Recent research has hypothesised
34 that most lakes drain in these cascading events (25) and that
35 pre-existing weaknesses in the ice may play a role (3, 24).
36 However, field studies capturing rapid drainage are limited and
37 have only previously been conducted on slow-flowing (~ 100 m
38 a⁻¹) land-terminating regions of the ice sheet (1–3, 11, 26). It
39 is unclear the extent to which knowledge of subglacial hydrology
40 at land-terminating margins may be applied to fast-flowing
41 marine-terminating systems (27) where supraglacial lakes are
42 equally numerous (18, 24).
43

44 Here, we present field measurements of the rapid drainage
45 of the supraglacial lake ‘Lake 028’ (70.57°N, 50.08°W; Fig. 1)
46 located ~ 30 km from the marine terminus of Store Glacier
47 (*Qarassap Sermia*) in West Greenland, at a site where annual
48 ice flow averages ~ 600 m a⁻¹. We combine data from repeat
49 Unmanned Aerial Vehicle (UAV) photogrammetry with *in-*

Significance Statement

We present the first *in-situ* records of a rapidly draining supraglacial lake in a fast-flowing sector of the Greenland Ice Sheet. Despite supraglacial lake drainage influencing ice sheet dynamics at a variety of scales, existing *in-situ* studies have been conducted exclusively at the slower, less dynamic land-terminating sector. We describe for the first time the scale and extent of dynamic response in a marine-terminating system, and identify (i) spatially distributed behaviour not previously observed in *in-situ* studies and (ii) interannual variation unique to fast-flowing glaciers. We propose that many lakes thought to drain slowly are in fact draining rapidly via hydrofracture. As such, rapid drainage events, and their net impact on ice sheet dynamics, may be being notably under-estimated.

T.R.C. and P.C. designed the study; T.R.C. collected and processed photogrammetry and analysed data.; S.H.D. collected and processed GPS ground station and pressure transducer data, with post-processing by T.R.C.; M.B. modelled subglacial routing; C.M.S. collected and processed seismic data; B.H. assisted with structural interpretation; M.R.J. assisted with photogrammetry; T.R.C. wrote the paper with input from all authors.

The authors declare no conflict of interest.

¹To whom correspondence should be addressed. E-mail: trc33cam.ac.uk or pc350cam.ac.uk

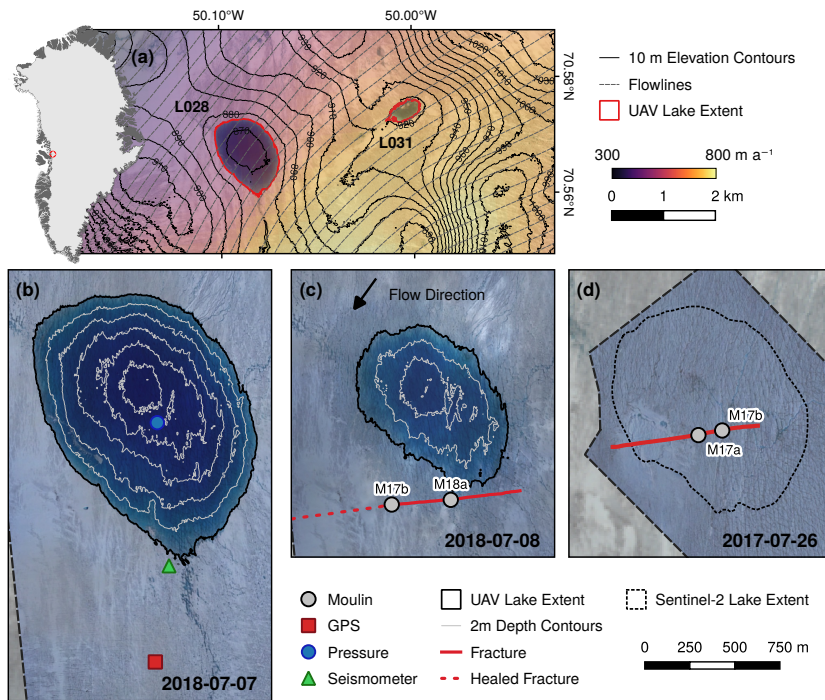


Fig. 1. (a) Location of Lake 028 and Lake 031 (red outlines). Sentinel-2 image from 2018-07-07 overlaid with the MEaSUREs 2017 velocity dataset (28) and contour lines from ArcticDEM (29) (inset: location of Store Glacier in Greenland). (b) Lake 028 on 2018-07-07, ~5 hours prior to the onset of drainage, with instrument locations highlighted. (c) Lake 028 on the 2018-07-08 ~4 hours after peak drainage, with ~1-km-long fracture marked in red, and moulins marked as white dots. (d) Bed of fully-drained Lake 028 on 2017-07-26, with maximum observed lake margin (from 2017-06-26) outlined with dashed black line.

50 *situ* geophysical observations from pressure transducer, dual-
 51 frequency GPS, and seismometers. The addition of high-
 52 resolution photogrammetry data allows the spatial distribution
 53 of dynamic response to be assessed, and aids detailed
 54 structural interpretation of the drainage event. We present
 55 observations at high spatial and temporal resolutions, describe
 56 the lake drainage mechanism, interpret the dynamic effects
 57 and structural history of the lake drainage, and discuss the
 58 larger-scale significance of the observed mode of lake drainage.

59 Results

60 **2018 Lake Drainage Event.** Records from a pressure transducer
 61 installed at the bed of Lake 028 on 2018-07-04 were converted
 62 into time-series of volume and discharge (Fig. 2a-b) using lake
 63 bathymetry derived from UAV photogrammetry (see supplementary
 64 text). These data indicate that in the three days prior to drainage,
 65 the volume of Lake 028 was increasing at a rate between 1-10 m³ s⁻¹.
 66 At its maximum extent on 2018-07-07, Lake 028 was 1.25 km² in area,
 67 7.3 × 10⁶ m³ in volume, and fed by three supraglacial streams. A
 68 single outflow channel emerged at the southern lake shore (Fig. 1b).
 69 The lake reached its maximum size immediately prior to drainage,
 70 which began on 2018-07-07 17:42 UTC (Fig. 2a). Rapid discharge
 71 (defined following (2) as >50 m³ s⁻¹) initiated at 18:32 UTC,
 72 accelerated notably at approximately 19:58 (Fig. 2b), and reached
 73 its peak (924 m³ s⁻¹) at 21:20 UTC. After this, discharge decayed
 74 exponentially. 23:22 UTC marked the end of rapid (Q > 50 m³ s⁻¹)
 75 drainage, which lasted ~5 hours in total. Lake volume continued to
 76 decline for the remainder of the record as flow into the moulin
 77 continued: at 2018-07-08 00:00, the lake volume was 2.2 × 10⁶ m³,
 78 but by 2018-07-24 18:00 was 3.1 × 10⁵ m³. A small (~200 m diameter)
 79 lake was still present in Sentinel-2 imagery by the end of the ablation
 80 season, and had frozen over by November 2018.

81 In addition to discharge measurements, we recorded ice
 82
 83

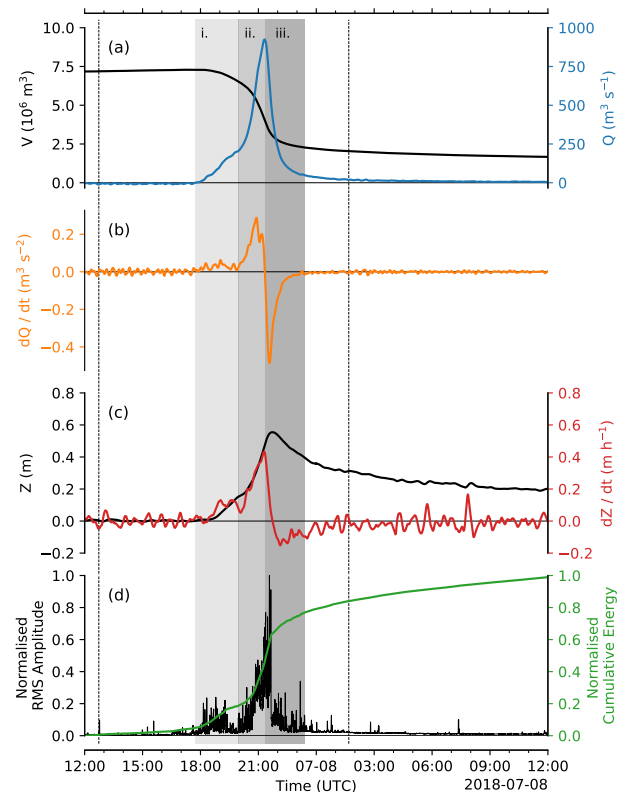


Fig. 2. Time-series of (a) lake volume (V) and discharge (Q); (b) rate of change of discharge (dQ/dt); (c) surface uplift (Z) and rate of uplift (dZ/dt); and (d) normalised root mean square (RMS) seismic amplitude, and normalised cumulative energy at Lake 028. Dotted lines at 12:45 and 01:40 mark the timing of pre- and post-flight drainage UAV surveys shown in Fig. 1b and c. Shading marks the three phases of rapid drainage outlined in the discussion. A version of this figure cropped to the time of rapid discharge is available as part of Supplemental Movie S1.

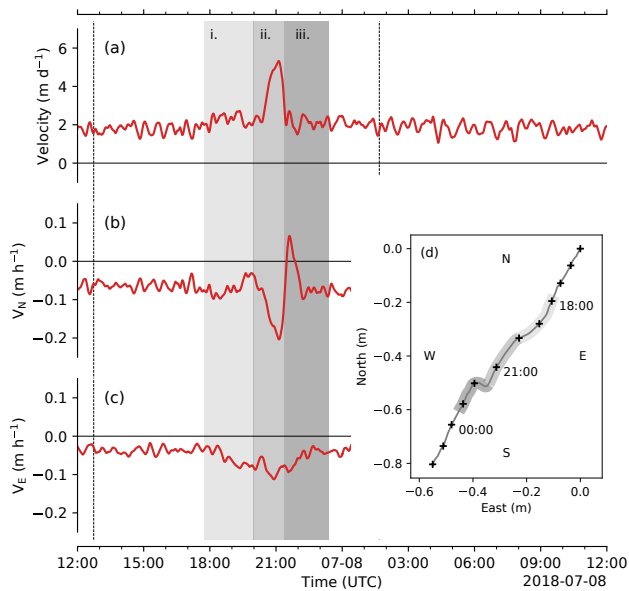


Fig. 3. Time-series of location data obtained from GPS instrumentation located ~ 750 m downflow of Lake 028 (Fig. 1b), including (a) resultant horizontal velocity and the (b) northerly (V_N) and (c) easterly (V_E) components of velocity, together with (d) mapped horizontal displacement between 2018-07-07 15:00 and 2018-07-08 02:00, with hourly locations marked with crosses. Dotted lines at 12:45 and 01:40 mark the timing of pre- and post-flight drainage UAV surveys shown in Fig. 1b and c. Shading marks the three phases of rapid drainage outlined in the discussion.

UTC, coincident with maximum negative discharge rate and peak seismic activity.

Spatially distributed uplift and ice flow dynamics. Repeat UAV photogrammetry captured at approximately daily intervals before and after the lake drainage event (See SI Appendix, Table S1) provides novel records of the spatial distribution of the ice sheet's response to drainage in the region surrounding Lake 028 (Table S1). An immediate post-drainage survey at 2018-07-08 01:45 UTC ~ 2 hours after the termination of rapid drainage – allow us to map drainage-induced uplift (Fig. 4a). We identify three distinct regions of uplift. The first major region of uplift (region A) was located surrounding the fracture, on the southwest side of the lake basin. A second major region of uplift (region C), was located at a distal site 4 km S-SE of the fracture. They are linked by a region of lower-magnitude uplift (region B).

Velocity fields are derived from repeat UAV surveys. We compare two velocity fields, one over the lake drainage period (2018-07-06–09) and one from a late-season control period (2018-07-18–24) to highlight regions of anomalous ice velocity during drainage (Fig. 4b). These data show that the short-term (on a scale of hours) acceleration observed in the immediate vicinity of Lake 028 (Fig. 3c) is not visible on a multi-day timescale. In contrast, considerable acceleration was observed at the distal site (region C), where ice velocity increased by up to 15% relative to the late-season control period. This suggests that ice velocity here was persistently elevated through the observation period, compared to only short-term acceleration around the lake site itself. This distal region also corresponds to an area of uplift in the elevation difference data.

Inception and propagation of fractures. The 2018 fracture was a direct continuation of a fracture formed during the complete rapid drainage of Lake 028 in 2017 (Fig. 1d). Two notable moulins occurred along the 2017 fracture (Fig. 5b): one larger (M17a in Fig. 5a) and one smaller (M17b in Fig. 5a), the latter of which became the dominant drainage moulin for the rest of the 2017 season. By 2018, this pre-existing fracture had advected ~ 500 m southwest (Fig. 5a; c), and both moulins, as well as the fracture, had closed. Between the 2018-07-04 and 2018-07-06, Lake 028 overtopped and began filling M17a (Fig. 5c, top-left inset). By the 2018 drainage event, the maximum extent of Lake 028 was coincident with the location of M17b (Fig. 5c): post-drainage, this moulin showed evidence of reactivation as it was no longer water-filled post-drainage (Fig. 5d, bottom-right inset). M17a must also have been reactivated, as it was empty of water post drainage (Fig. 5c, top-left inset).

Extending from M17b, the western extent of the 2018 fracture was dominated by uneven edges and grabens (Fig. 5e). This section of the lake bed is also a region where a number of smaller, pre-existing surface crevasses occur (on the order of 10 m long and 0.5 m wide). The edges of the western extent of the 2018 fracture can be matched directly to these pre-existing crevasses (red lines in Fig. 5d), suggesting that the crevasses were exploited during drainage to form the larger fracture. The eastern extent of the 2018 fracture was typified by clean, linear fracturing (Fig. 5e), an appearance distinct from the western extent.

The orientation of the fractures in both years was at

84 uplift (Fig. 2c), seismic activity (Fig. 2d), and horizontal ice
 85 velocity (Fig. 3) using a GPS and seismometer located to the
 86 south of the lake (Fig. 1b). At approximately 18:30 UTC,
 87 coincident with the start of rapid ($Q > 50 \text{ m}^3 \text{ s}^{-1}$) drainage, ice
 88 uplift initiated at a rate of $\sim 0.1 \text{ m h}^{-1}$. This rate increased,
 89 in tandem with discharge, to a maximum rate of $\sim 0.4 \text{ m h}^{-1}$
 90 at 21:17 (contemporaneous with maximum discharge). Peak
 91 surface uplift of 0.55 m occurred at 21:43 UTC. Subsequently,
 92 the ice surface did not return to a pre-drainage elevation, in-
 93 stead settling ~ 0.2 m above pre-drainage levels (Fig. 2c) for
 94 the rest of the summer melt season. Trends in seismic data are
 95 consistent with those in discharge and surface uplift records.
 96 Following low-level (0-0.2 normalised RMS amplitude) activ-
 97 ity in the initial drainage period, activity accelerated rapidly
 98 after 19:58, reaching a maximum amplitude at 21:34 UTC
 99 (coincident with maximum deceleration in discharge), at which
 100 point seismic activity returned abruptly to levels < 0.3 for the
 101 remainder of the drainage period. Ice velocity was relatively
 102 consistent until 20:20 UTC, at which point rapid acceleration
 103 was observed, from a background velocity of $\sim 2.0 \text{ m d}^{-1}$ to a
 104 peak of 5.33 m d^{-1} at 21:07 UTC (Fig. 3a). Termination of
 105 the event was equally rapid, and by 21:27 UTC velocities had
 106 returned to normal levels. However, this resultant velocity
 107 hides anomalous directional movement (Fig. 3b–d). In the
 108 early stage of drainage (prior to the step accelerations ob-
 109 served in other data at $\sim 20:00$ UTC), the ice velocity trended
 110 in a westward direction (parallel with fracture orientation),
 111 unaccompanied by any significant change in magnitude. Coin-
 112 cident with the period of most rapid drainage, an anomalous
 113 southward displacement initiated (perpendicularly away from
 114 the fracture), peaking at a rate of 0.2 m h^{-1} at 21:07 UTC.
 115 Following this, a sharp northward anomaly occurred at 21:36

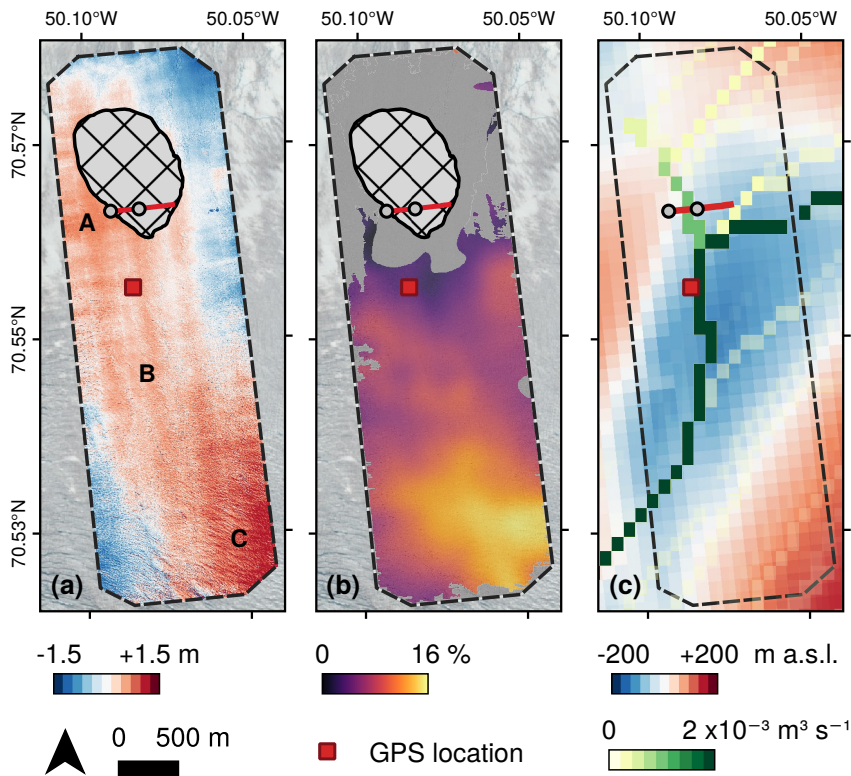


Fig. 4. (a) Absolute uplift post-drainage at 2018-07-08 01:44 relative to 2018-07-06 16:39 control, with regions A, B, and C referred to in the text labelled. (b) Relative acceleration over the period 2018-07-06–09 relative to 2018-07-18–24 control. The grey region marks area of insignificant change based on estimated uncertainty (see methods). (c) Modelled water routing, showing contours of discharge following an input of water to the system.

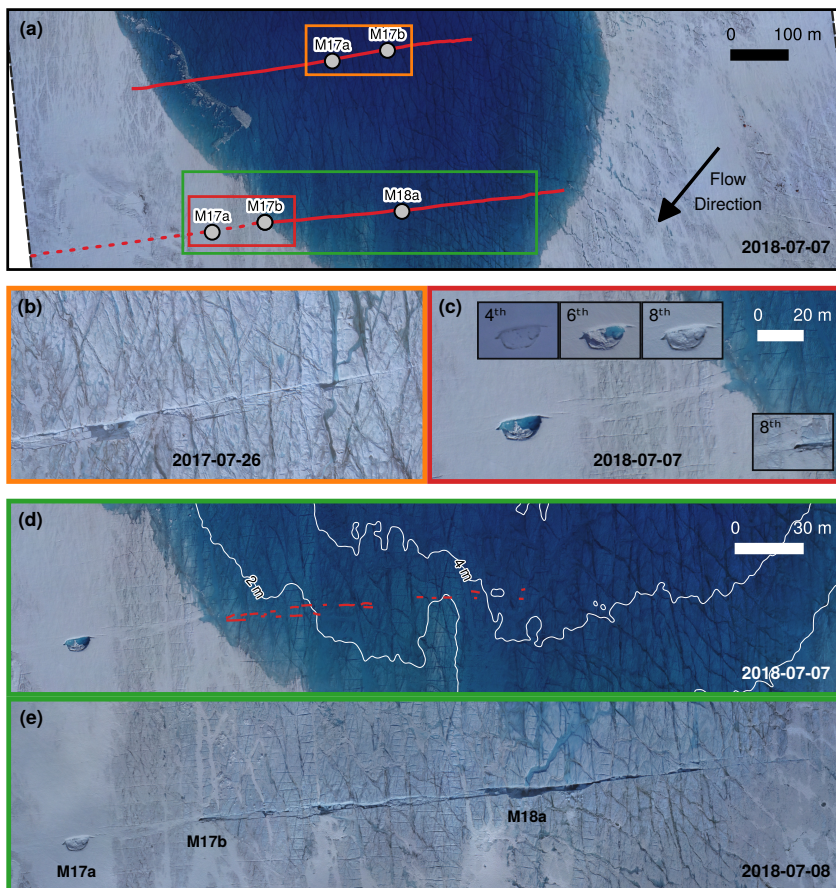


Fig. 5. UAV orthophotos of Lake 028 identifying key geomorphological features. (a) Locations of the main drainage fracture (black lines) in 2017 (top) and 2018 (bottom) are marked, along with associated moulins. Dashed black line marks the location of the healed 2017 crevasse in 2018. Coloured boxes indicate locations of panels b–e. (b) The 2017 crevasse and associated moulins 17a and 17b in 2017. (c) 2017 crevasse and associated moulins on 2018-07-07 immediately prior to drainage. The insets show moulin 17a on 2018-07-04, 2018-07-06, and 2018-07-08 (top left) and moulin 18a on 2018-07-08 after drainage (bottom right). (d) Region of Lake 028 subsequently fractured on 2018-07-07, prior to drainage. 2m depth contours are marked in white and crevasses exploited during drainage are in red. (e) Fracture of Lake 028 on 2018-07-08.

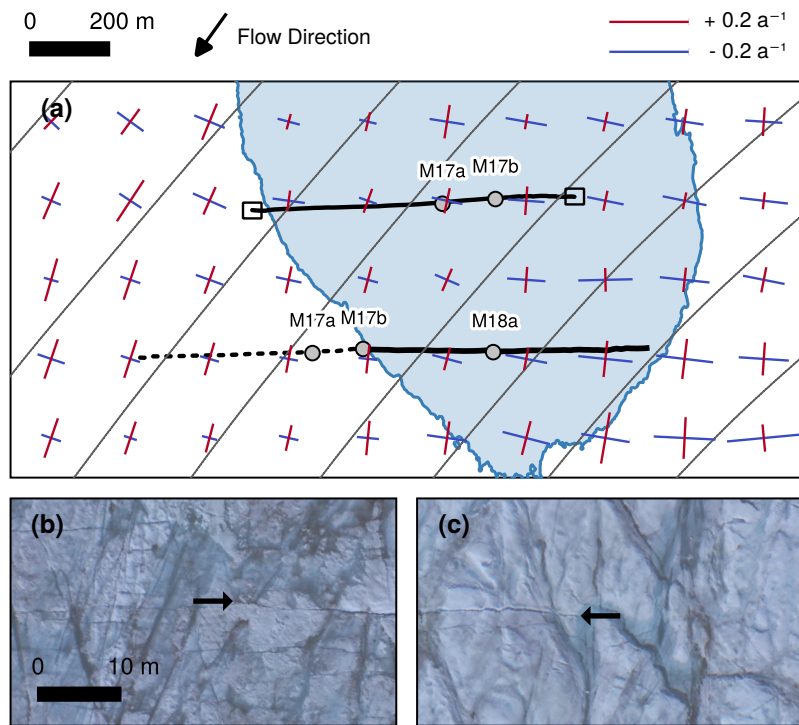


Fig. 6. (a) Surface principal strain rates (red and blue lines) derived from 2017 annual MEASUREs velocity data (28). 2018-07-08 maximum lake area is marked in blue, and flowlines are marked in grey. Black lines define the drainage fracture in 2017 (top) and 2018 (bottom), with the dotted line showing the location of the healed 2017 crevasse in 2018. Black boxes, from left to right, mark locations of UAV orthophotos in panel (b) showing presence of crevasses surrounding western edge of fracture, and (c) showing lack of crevasses around eastern edge of fracture. Black arrows identify the fracture limit.

176 $\sim 45^\circ$ to the direction of flow. Comparing this orientation
 177 to principal strain rates (Fig. 6a) shows that the fractures
 178 occurred perpendicular to the direction of first principal strain,
 179 indicating that the drainage fracture is a Mode I extensional
 180 fracture. In 2017, there were no obvious closed moulin or
 181 healed fractures to exploit. Instead, the fracture most likely
 182 initiated at its western edge, where numerous small surface
 183 crevasses occur due to the extensional strain regime (Fig. 6b)
 184 that could be exploited by hydrofracture. This hydrofracture
 185 could then propagate into the compressive lake basin due to
 186 inflow of water, first from the supraglacial stream network
 187 along the western lake shore and ultimately from the lake it-
 188 self, leading to full column penetration by hydrofracture. The
 189 compressional strain regime on the northeastern (i.e. upflow)
 190 side of the lake (Fig. 6a), evidenced by a lack of crevasses in
 191 the area (Fig. 6c), is likely to have limited the eastern
 192 extent of the hydrofracture in both 2017 and 2018.

193 Discussion

194 **Lake drainage mechanism.** Observational evidence suggests
 195 that the drainage of Lake 028 in July 2018 initiated via the re-
 196 filling of a closed moulin formed during the 2017 lake drainage,
 197 and subsequent reactivation of the 2017 hydrofracture. Be-
 198 tween UAV surveys on 2018-07-05 (02:00) and 2018-07-06
 199 (16:40) Lake 028's shoreline reached the location of the former
 200 moulin M17b. At this point, neither M17a nor M17b was open,
 201 as evidenced by the filling of moulin M17a between 2018-07-06
 202 (16:40) and 2018-07-07 (12:45) (Fig. 5c, inset). In the hours
 203 prior to rapid drainage, minor seismic activity began (Fig.
 204 2d), indicative of the episodic hydro-mechanical re-opening of
 205 the moulins. In the post-drainage survey (2018-07-09 16:15),
 206 these moulins were empty (Fig. 5d, inset), indicating that they
 207 had connected hydraulically, most likely to the glacier's bed,

during the drainage event. Lake drainages have previously
 208 been proposed to exploit pre-existing moulins (2, 3). Evidence
 209 suggests that water entering the subglacial system through
 210 pre-existing moulins can trigger hydrofracture by inducing
 211 localised acceleration and hence a transient extensional flow
 212 regime in a 'precursor' event (3, 30). However, there is no evi-
 213 dence of precursory acceleration or surface-to-bed connection
 214 at Lake 028. Furthermore, there is no evidence of any pre-
 215 cursory uplift indicating a triggering upstream drainage event
 216 (2, 25). We suggest that high background tensile stresses were
 217 likely sufficient for a surface-to-bed connection to commence
 218 as soon as the lake overtopped the pre-existing moulin. Taking
 219 the previously studied Lake F (2) as a contrasting example,
 220 first principal strains (See SI Appendix, Fig. S1) are an order
 221 of magnitude lower than at Lake 028 (Fig. 6a), and are not
 222 clearly aligned with fracture direction, suggesting that back-
 223 ground stresses do not exert a strong control in slow-flowing
 224 regions. This observation sheds new light on the proposition
 225 that supraglacial lakes can drain in a 'cascading' chain-reaction
 226 (25). While this mechanism may explain how hydrofracture in
 227 low stress regimes can occur in response to upstream drainage,
 228 there is still no explanation for the triggering of the upstream
 229 events themselves. We propose that lakes like Lake 028 can
 230 act as 'trigger lakes', i.e. situated in stress regimes where the
 231 simple intersection of an expanding lake with a pre-existing
 232 moulin is enough to trigger hydrofracture. In contrast, lakes
 233 from previous *in-situ* studies may be considered 'response
 234 lakes', i.e. lakes which require a precursory event in order to
 235 drain.

Following drainage initiation, we interpret geophysical activi-
 237 ty as representing three clear phases (2): Phase i (17:42–19:58),
 238 drainage onset, Phase ii (19:58–21:22), fracture opening, and
 239 Phase iii (21:22–23:22), fracture closing (these phases are high-
 240 lighted in Figures 2 and 3). Phase i began with the initiation
 241

242 of drainage at 17:42. It was characterised by discharge, uplift,
243 acceleration, and seismic activity that was relatively low compared
244 to later drainage. We suggest that, in phase i, water
245 was delivered to the bed exclusively through the reactivated
246 M17b, and discharge rates increased via the mechanical or
247 thermal erosion of the moulin and the remnant 2017 fracture.
248 This mechanism would explain the distinctive morphology
249 of the western extent of the 2018 fracture, characterised by
250 the exploitation of pre-existing crevasses to form distinctive
251 graben structures (Fig. 5e).

252 Phase ii of Lake 028's drainage began at 19:58 with a
253 step increase in discharge (Fig. 2a–b). A sudden and rapid
254 southwards ice displacement is visible in the GPS record at
255 this time (Fig. 3b). Given the GPS location 900 m south
256 of the east-west oriented fracture, we interpret this as strong
257 evidence of mechanical fracture opening (2). We interpret
258 the clean, linear fracturing distinctive of the eastern half of
259 the 2018 fracture (Fig. 5f) as indicating that the fracture
260 propagated via hydrofracture rather than by mechanical or
261 thermal erosion. This hydrofracture mode began once the
262 fracture propagated into depths greater than 4 m (Fig. 5d).
263 As such, this depth likely represents the point at which – in
264 this particular setting – hydrostatic pressure was sufficient to
265 initiate full-column hydrofracture. The westernmost extent of
266 the new hydrofracture was also coincident with the location of
267 M18a, suggesting that hydrofracture initiation allowed M18a
268 to connect to the bed. The formation of M18a at this point
269 would have coincided with, and thus explains, the dramatically
270 increased water discharge from Lake 028 at the beginning of
271 phase ii (Fig. 2a). This inference is supported by a marked
272 increase in the intensity of seismic activity in this period
273 (Fig. 2d), as well as peak horizontal velocity, likely forced by
274 hydraulic jacking. Phase ii terminated at the point of peak
275 discharge (Fig. 2a), which was coincident with the beginning
276 of fracture closure as indicated by the GPS data (Fig. 3b).

277 Phase iii is defined from the beginning of negative dQ/dt
278 at 21:22. Throughout this period, decreasing discharge was
279 observed: fourteen minutes into the period, at 21:34 UTC,
280 maximum deceleration in discharge occurred (Fig. 2b). This
281 timing coincided with a maximum in seismic activity, and
282 three minutes later (21:37 UTC), the northwards anomaly in
283 the GPS record reached a maximum (the northwards anomaly
284 occurred from 21:28 – 22:14 UTC). We interpret these closely
285 spaced events as strong evidence of rapid fracture closure
286 occurring in this period. This period of lake drainage was
287 captured with 10 s time-lapse photography from a location to
288 the southeast of the lake (See Supplemental Movie S1). This
289 footage shows that early Phase iii, when discharge declined
290 most rapidly (~21:30–22:15 UTC), occurred simultaneously
291 with the lake level dropping beneath that of the fracture. At
292 this point, a plume of water vapour developed at the fracture
293 mouth as the fracture transitioned from being fully water-
294 filled to a water-air mix. When the fracture was filled to
295 the surface, water pressure exceeded ice overburden pressure
296 and allowed the fracture to remain open. As water content
297 in the fracture reduced, water pressure also lowered and led
298 to fracture closure, lower water inputs, and the subsequent
299 cessation of uplift and acceleration. Therefore, the triggering
300 event for termination of the short-term dynamic response to
301 drainage was the drop in lake water level beneath that of the
302 fracture elevation.

303 Although we define the end of Phase iii at 23:20 based on
304 the termination of drainage $>50 \text{ m}^3 \text{ s}^{-1}$, there is a long tail
305 to observed hydrological activity. By the time of the post-
306 drainage UAV survey at 2018-07-08 01:45 UTC, the edge of
307 the lake was still proximal to the fracture, and eight separate
308 channels were flowing into the fracture. By the time of the
309 subsequent UAV survey (2018-07-08 15:15 UTC), only three
310 channels remained, and 24 hours later (2018-07-09 16:15 UTC)
311 one supraglacial channel and associated moulin remained,
312 which dominated for the rest of the melt season.

313 The elevation time-series from the GPS located to the south
314 of the lake shows a persistent post-drainage surface uplift of
315 $\sim 0.2 \text{ m}$ above the pre-drainage level (Fig. 2c). Previous studies
316 have reported a similar phenomenon (1–3, 11), interpreting it
317 as transient water storage at the bed or reverse dip/slip faulting
318 (2). We did not observe any evidence of reverse faulting, so we
319 favour the hypothesis that the persistent uplift is indicative of
320 changes to the subglacial system. Substantial surface lowering
321 ($>1 \text{ m}$) was observed in the northeast area of the study site (Fig.
322 4a). Given this lowering was spatially confined and observed
323 over only ~ 33 hours, it cannot be explained by surface melt
324 alone. We hypothesise that this excess lowering could relate
325 to a loss of subglacially stored water or sediment in this region
326 following lake drainage. Hence, this pattern of persistent uplift
327 downstream of the lake and surface lowering upstream could
328 be explained some combination of rerouting of the subglacial
329 hydrological system (31) leading to increased water storage
330 beneath the location of the GPS, and/or the redistribution of
331 subglacial sediment during rapid lake drainage (32).

Spatial distribution of dynamic response. The northwest
332 region of ice uplift (Region A in Fig. 4a) was located proximal
333 to the fracture. We interpret this to be a result of hydraulic
334 jacking in the region surrounding the direct injection of water
335 to the bed. In modelling studies, this has been interpreted
336 as a turbulent sheet or water 'blister' (10) spreading radially
337 from the moulin injection point. Measured uplift here peaked
338 at $\sim 0.8 \text{ m}$, which is consistent with previous studies (1–3, 11).
339 Uplift was focused to the southwest of the lake centre (Fig.
340 4a), in contrast to previous studies of alpine and ice sheet lake
341 drainages which have speculated that ice uplift is greatest near
342 the centre of lakes (1, 2, 9). This likely reflects the location
343 of surface-to-bed hydrological connections: the fracture and
344 moulins reported here were located offset in this direction from
345 the lake centre, whereas previous studies of lake drainages have
346 been of lakes that hydrofractured at their centre.
347

348 The area of lower-magnitude uplift observed in Region B
349 (Fig. 4a), correlates with the predicted peak subglacial dis-
350 charge pathway (Fig. 4c) derived from modelled subglacial
351 hydrological routing (see methods). We interpret uplift at
352 Region B to have resulted from hydraulic jacking – and subse-
353 quent concentration of water – along preferential flow routes
354 as lakewater was routed away from the injection site. The > 1
355 km wide region over which this uplift is distributed leads us
356 to envisage the subglacial hydrology as a turbulent sheet or
357 blister rather than a single efficient channel. Uplift similar
358 to that observed at Region B has not been observed previ-
359 ously, but our interpretation agrees with modelling results
360 (10), which found that large and efficient subglacial channels
361 do not form rapidly as a result of rapid lake drainage. Instead,
362 water flows downstream once blister growth is restricted by
363 basal topography.

364 In contrast, the distal area of high-magnitude uplift located
365 in Region C has not been observed or predicted previously.
366 It does not correlate with subglacial flow routes predicted
367 by modelled hydrological routing, which continues along the
368 bedrock trough (Fig. 4c). One option to explain this di-
369 vergence between the inferred and modelled water routing
370 pathways could be due to errors in BedMachine v3, which
371 has reported uncertainty in excess of 50 m around Region
372 C. However, whilst this would explain a simple divergence
373 between inferred and modelled pathways, it does not explain
374 why the uplift of Region C is greater than at regions A or B.
375 We suggest that (assuming the modelled hydrological routing
376 is correct), Region C constitutes an area of less efficient sub-
377 glacial drainage, which resulted in higher water retention and
378 enhanced hydraulic jacking.

379 The pattern of water routing described above may also
380 explain why ice acceleration over the drainage period (Fig. 4b)
381 was concentrated in region C, whilst acceleration elsewhere,
382 particularly at the lake site itself, was less pronounced. The
383 velocity field in Fig. 4b represents a three-day period, and,
384 as such, the significant short-term (\sim hours) accelerations ob-
385 served in the GPS data are likely averaged out. If the northern
386 and central sections of the drainage system became more effi-
387 cient following lake drainage and moulin formation, then there
388 would be limited dynamic response in these areas throughout
389 most of the velocity observation period. Meanwhile, at region
390 C, an inefficient drainage system may have allowed continuing
391 dynamic response to variations in water input. Dynamic re-
392 sponse may have been greater than pre-drainage, as meltwater
393 from the entire catchment area was then being delivered effi-
394 ciently to the bed via moulin M18a, increasing discharge rates.
395 Hence, the most sensitive response to a lake drainage event on
396 the timescale of days-weeks was not necessarily at the location
397 where water is injected at the bed, but instead governed by
398 the subglacial pathway taken by the water as well as by the
399 physical state of the hydrological system at the bed. These
400 observations align with regional-scale remote sensing data (33),
401 which identified that areas of peak acceleration through a melt
402 season coincide with bedrock troughs and intervening ridges,
403 where hydraulic gradients are weak and the rate at which
404 turbulent flow enlarges conduits through melting is low. The
405 study identified these factors as particularly strong in areas
406 where bedrock structures are not well aligned with regional
407 ice flow – as occurs at region C (Fig. 4c). *In-situ* studies
408 of lake drainages frequently locate ground instrumentation
409 close to the lake site (1–3, 26). For better quantification of
410 distributed dynamic impacts of lake drainage, future work may
411 wish to also study potential distant ‘hotspots’ as informed by
412 low hydraulic gradients in the basal environment.

413 **Influence of structural history on lake drainage mode.** In re-
414 cent history, Lake 028 has displayed three different behaviours.
415 Between 2011–2016, the lake did not drain rapidly at all, and
416 froze over at the end of each melt season. In 2017, the lake was
417 able to drain completely through a newly formed hydrofracture
418 located in the lake centre. We hereafter call this a ‘primary’
419 hydrofracture. In 2018, the lake drained by reactivating a
420 fracture formed during the previous year’s drainage event. We
421 hereafter call this a ‘secondary’ hydrofracture. However, as
422 the fracture had advected \sim 500 m southwest and was oriented
423 45° to the flow direction, the fracture did not cut across the
424 deepest section of the lake and, as such, the lake failed to

425 drain completely. Here, we make a further distinction between
426 ‘complete’ and ‘partial’ rapid drainage. By 2019, any 2018
427 moulins had advected out of the lake basin entirely and, as
428 such, secondary hydrofracture could not occur again: instead,
429 in 2019, Lake 028 again underwent complete rapid drainage
430 by primary hydrofracture (See SI Appendix, Fig. S2).

431 The concept of rapid drainage via the reactivation of pre-
432 existing crevasses and moulins has been proposed previously
433 in slow-moving ($\sim 100 \text{ m a}^{-1}$), land-terminating sectors of the
434 Greenland Ice Sheet at Lake F (2) and North Lake (3). How-
435 ever, Lake 028 exhibits markedly different behaviour from
436 previous *in-situ* studies on two counts. The first is that of in-
437 terannual behaviour. Manual inspection of 32 years of available
438 Landsat and Sentinel-2 satellite imagery between 1985–2018
439 suggests that Lake 028 rapidly drained 12 times (38% of years),
440 of which two (2006 and 2018, 17% of drainages) show clear
441 evidence of ‘secondary’ drainage features (See SI Appendix,
442 Fig. S3). Meanwhile, for a parallel analysis of ten years (2009–
443 2018) of data, Lake F (2) and North Lake (3) fully drained
444 every year, except for one year each (2011 at Lake F and
445 2014 at North Lake) where the lakes did not fill at all. Our
446 interpretation of these years is that moulins from the previous
447 year remained open, preventing the lakes from forming.

448 The second difference is the extent of drainage. North
449 Lake and Lake F are both described as reactivating previous
450 moulins/fractures (2, 3), and hence would be classified here as
451 draining via secondary hydrofracture. However, they undergo
452 complete rapid drainage, whereas Lake 028 only undergoes
453 partial rapid drainage. We suggest that these differences in
454 behaviour can be explained by two compounding factors: (i)
455 the lower ice velocity in land-terminating sectors of the ice
456 sheet ($\sim 100 \text{ m a}^{-1}$) means that relict moulins and fractures
457 do not advect out of the lake bed after only one year, increas-
458 ing the chance of drainage via secondary hydrofracture; and
459 (ii) fractures at Lake F and North Lake are aligned parallel
460 with flow direction, meaning that year-on-year, the reactivated
461 fracture intersects the approximate lake centre for consecutive
462 years, allowing for complete rapid drainage. Controls on the
463 orientation of lake drainage fractures in a land-terminating
464 setting have been previously considered in a modelling context
465 (25), where the variable direction of flow routing at the bed
466 was considered to be the primary influence on fracture orien-
467 tation. Here, we show that background stress regime can have
468 strong control on fracture orientation, and as such identify the
469 important role of pre-existing fractures (in 2018) and crevasses
470 advected into the lake basin (in 2017) on fracture orientation,
471 and therefore also on the degree to which rapid lake drainage
472 is complete or partial.

473 As a result of the two factors described above, North Lake
474 and Lake F consistently experience complete rapid drainage
475 via secondary hydrofracture (2, 3). In contrast, lakes like Lake
476 028, which (i) exist in fast-flowing sectors of the ice sheet where
477 structural weaknesses are rapidly advected outside the lake-
478 bed; and (ii) occur in strain regimes (such as regions of rapidly
479 accelerating ice, or zones of shear) that do not create flow-
480 parallel fractures, make secondary hydrofracture uncommon.
481 Instead, in years without relict moulins or hydrofractures (e.g.
482 2017), primary hydrofracture must occur by exploiting only
483 surface crevasses, potentially aided by other factors such as
484 the drainage of neighbouring lakes that trigger short-term
485 perturbations in the regional stress/strain regime (17, 25). In

486 the absence of these factors, rapid drainage may not occur
487 at all (e.g. 2011–2016). As a result, lake drainages may
488 be less common (on an individual, interannual level) in fast-
489 flowing sectors of the ice sheet. Given that multi-year remote
490 sensing studies have found that most lakes that exhibit rapid
491 drainage behaviour do so less than 50% of the time (22, 23),
492 Lake 028 could provide a representative model for these lakes'
493 interannual behaviour.

494 The above discussion has implications for remote sensing
495 studies designed to identify rapidly draining lakes automati-
496 cally. The nature of partial rapid drainage appears site-specific,
497 but if widespread in fast-flowing sectors of the ice sheet then
498 automated lake identification routines in remote sensing stud-
499 ies are highly likely to be misclassifying rapid lake drainages
500 where, like Lake 028 in 2018, only partial drainage occurs.
501 Many classifications use a threshold of 80–90% loss in area
502 (18, 23, 34) or volume (17, 35, 36) within a defined period
503 (often 2–6 days) to qualify as a rapid drainage event (i.e.
504 drainage via hydrofracture). In this binary classification, lakes
505 that only drain partially are also assumed to drain slowly (on
506 the scale of ~days) into pre-existing moulins via fast incision
507 of a supraglacial outlet channel (11, 37, 38). However, only
508 41% of area (1.25 to 0.51 km²) and 66% of volume (7.1 to
509 2.3 × 10⁶ m³) was lost overnight from Lake 028, meaning that
510 this drainage would not be classified as a rapid/hydrofracture-
511 induced drainage by published identification routines, whereas
512 in situ records of the event clearly show that it meets this
513 criterion in terms of flux and hydrological connection to the
514 bed. Identifying the mode of drainage of Lake 028 in medium-
515 resolution optical imagery can be difficult even when manual
516 identification is used. A key identifying feature is that the
517 configuration of surface outlet channel direction and fracture
518 orientation is such that secondary drainage cuts off the outflow
519 channel, which is present for the full season in years with no
520 drainage (See SI Appendix, Fig. S4). It is likely, then, that ex-
521 isting remote sensing routines are underestimating the number
522 of actual rapid lake drainage events. This has important conse-
523 quences when subglacial hydrological models are forced in part
524 by these remotely sensed observations (e.g. 21, 25), as these
525 models are correspondingly underestimating the total water
526 volume rapidly delivered to the bed, as well as, later in the
527 season, the locations at which water is being delivered. The
528 identification of hydrofracture is known to be highly sensitive
529 to the precise criteria applied (18), and these findings further
530 highlight a need for more nuanced remote sensing routines to
531 detect drainages.

532 If rapid lake drainages are more extensive than previously
533 thought, wider implications exist for Greenland ice sheet hy-
534 drology and dynamics as lake hydrofracture is thought to
535 be the primary control on moulin density and extent (14).
536 Moulins are the primary mechanism by which rapid lake
537 drainages can have a longer-term (weeks-years) influence on
538 subglacial hydrology: while supraglacial lakes may contain
539 only ~3% of the total melt season runoff volume, a further
540 ~21% has been estimated to drain through newly opened
541 moulins created by hydrofracture events, and an additional
542 ~15% through pre-existing moulins created during previous
543 melt seasons (38), which can remain active for many years in a
544 row (15). Furthermore, moulins act to concentrate meltwater
545 delivery spatially, to a point source, and also temporally, as
546 water transfer via moulin is nearly instantaneous compared to

547 drainage through crevasse systems (39). Our finding that par-
548 tial lake drainages also occur through hydrofracture indicates
549 that many lakes previously inferred to drain by overtopping or
550 channel incision (11), in fact are establishing moulins and hy-
551 drological connections to the bed (14). Consequently, a larger
552 portion of the subglacial drainage system could be subject to
553 a persistent, yet also highly variable meltwater supply from
554 the surface. This may mean that, early in the melt season,
555 more of the basal system is subject to pulses in supply (from
556 events such as high-melt days and rainfall) that are capable
557 of overwhelming transmission capacity and therefore enhance
558 basal sliding (39, 40). Later in the season, concentrated melt-
559 water delivery could also accelerate the formation and spatial
560 extent of efficient channels, which have a stabilising effect on
561 the ice sheet's flow (5, 14, 40).

562 Given the relationship between primary and secondary
563 hydrofracture, we argue that consecutive years of rapid lake
564 drainage are more likely in slow-moving sectors of the ice sheet.
565 In fast-flowing sectors, full-depth fractures are rapidly advected
566 out of lake basins and therefore new hydrofractures must
567 exploit shallower surface crevasses, facilitated by a stronger
568 extensional stress regime. Conversely, this implies that if a
569 lake can hydrofracture just once in a slow-flowing regime, the
570 presence of relict fractures and moulins makes it easier for
571 rapid drainage to reoccur year-on-year. This is a relevant
572 factor in discussions of interannual dynamic changes in the
573 land-terminating ablation zone (8), but may be especially
574 important in inland sectors of the ice sheet (7), where surface-
575 to-bed connections have been proposed to be less likely (41).
576 However, if decadal-scale dynamic changes to the ice sheet
577 induce even limited extensional crevassing further inland, one
578 lake drainage via primary hydrofracture may be enough to
579 induce consistent secondary hydrofracture in further years, as
580 relict features are unlikely to advect out of the lake bed within
581 only a few seasons.

582 Conclusions

583 Fast-flowing, marine-terminating glacier hydrology represents
584 a key uncertainty in predictions of sea level rise (27), and the
585 long-term response of marine-terminating glaciers to climate
586 change and lake expansion remains unknown. Our results
587 contribute better observational understanding of ice sheet
588 hydrology and dynamics by identifying key differences between
589 supraglacial lakes on fast-flowing and slow-flowing sectors of
590 the ice sheet. As rapid, hydrofracture-induced drainage can
591 occur even at partially draining lakes in fast-flowing sectors,
592 the increased potential density of surface-to-bed connections
593 (14) has implications for subglacial drainage efficiency in both
594 the early melt season (as a positive feedback to ice velocity)
595 and in the long term (as a mitigating effect to increased surface
596 melt). The observation that hydrofracture can occur without
597 any precursory hydrologically-induced basal slip (3) identifies
598 for the first time a triggering mechanism for cascading lake
599 drainage events (25), which means that the style of drainage
600 observed here could be important in initiating a chain reaction
601 of meltwater delivery to the bed. Furthermore, an increased
602 understanding of the necessary conditions behind year-on-year
603 hydrofracture has significance when considering meltwater
604 delivery to the bed in inland regions, which currently represent
605 a large unknown in predicting future dynamic change of the
606 ice sheet (7, 41). Given the ongoing dominance of mass loss

607 via dynamic losses from the marine-terminating Greenland Ice
608 Sheet (42), improving our understanding the unique hydrology
609 and dynamics of these sectors is key to constraining mass
610 balance predictions into the 21st century.

611 Materials and Methods

612
613 By the 2018-07-07 drainage event, Lake 028 was instrumented
614 with a GPS receiver, seismometer, and pressure transducer sensor
615 (Fig. 1a). A dual-frequency GPS was installed ~600 m upstream of
616 the lake in July 2017, and by July 2018 had advected into a position
617 immediately south of the lake. A seismometer was installed in
618 May 2018, and a water-level sensor on 2018-07-04. From this date,
619 regular UAV surveys (See SI Appendix, Table S1) were performed
620 over the lake and surrounding environments. Lake 028 drained three
621 days later, on 2018-07-07 between approximately 18:00 and 23:00
622 (Fig. 1b). All times are expressed in Coordinated Universal Time
623 (UTC).

624 **Pressure Transducer.** A pressure transducer (Solinst 3001 Levelger)
625 was installed on the 2018-07-04, logging at 2-minute intervals.
626 The record was corrected for changes in atmospheric pressure using
627 hourly surface pressure data from ERA-5 reanalysis data (43).
628 A depth-volume relationship was established using a bathymetry
629 map of the lake at 0.2 m resolution produced from depth-corrected
630 UAV-derived DEMs (see supplementary text). Time series of lake
631 volume (V), discharge (Q), and rate of change in discharge (dQ/dt)
632 were calculated from this depth-volume relationship.

633 **GPS.** We measured ice surface velocity and uplift using a Trimble
634 NetR7 dual-frequency Global Positioning System (GPS) receiver
635 logging continuously at 0.1 Hz using a Trimble Zephyr Geodetic
636 III Antenna. We processed dual-frequency GPS data kinematically
637 (44) using the differential carrier-phase positioning software, Track
638 v. 1.30 (45, <http://geoweb.mit.edu/gg/>) and final precise ephemeris
639 from the International GNSS Service (46). The data were processed
640 against an off-ice reference system, a Trimble NetR9 receiver located
641 on *Qarassap Nunata* (70.4 °N, 50.7 °W). We discarded solutions
642 where carrier-phase ambiguities were not fixed to the current integer,
643 where an insufficient number (<4) of double-difference calculations
644 were made, or where position standard deviation exceeded 0.035 m.
645 High-frequency noise was filtered with a two-pole, low-pass Butterworth
646 filter with a 30-minute cutoff period (47). This 30-minute
647 window was chosen based on a worst case horizontal positional
648 uncertainty of 0.035 m and a base ice velocity of ~650 m a⁻¹, fol-
649 lowing from which assumptions the period over which velocities
650 can be resolved is ~0.5 hours. Uncertainty was calculated based
651 on a conservative estimate of the positional uncertainty of ±1 cm
652 propagated through the velocity calculation.

653 **Seismometers.** Seismic monitoring was conducted using a passive
654 HG-7 10 Hz geophone deployed in a shallow (3 m) borehole. Record-
655 ings were taken at 400 sps using a DiGOS DATA-CUBE. Changes
656 in seismic energy were studied using the normalised RMS ampli-
657 tude. Data were decimated to 100 sps and a 2-pole, zero-phase
658 bandpass filter (10-50 Hz) was applied to eliminate instrument
659 and high-frequency noise. The normalised RMS amplitude was
660 then calculated for 60 s time windows. The normalised cumulative
661 amplitude was also calculated to identify rapid changes in seismic
662 energy.

663 **UAV Photogrammetry.** We acquired aerial imagery using a custom
664 2.1 m fixed-wing UAV (48). The survey plan, designed with the
665 assistance of the 5 m resolution ArcticDEM mosaic, provided a
666 consistent flight altitude of ~450 m, with a ground-level image
667 footprint of ~660 x 440 m and a ground sampling distance (GSD)
668 of 11 cm. Digital imagery was acquired by a Sony α6000 24 MP
669 camera with a fixed 16 mm lens. Imagery was captured every 90 m
670 along flight lines spaced 240 m apart, in order to achieve an >80%
671 (>60%) overlap along (between) flight lines for photogrammetry
672 purposes. The point cloud was geolocated via GNSS-assisted aerial
673 triangulation, using an on-board Emlid Reach single-frequency
674 carrier-phase GPS receiver (recording at 10 Hz) postprocessed using

675 the Emlid RTKLIB b27 software suite against 10 Hz data from a
676 ground-based NetR9s (48). A total of 11 surveys were performed
677 over the study period between 2018-07-05 and 2018-07-28 (See SI
678 Appendix, Table S1).

679 Photogrammetric outputs were calculated from images and camera
680 positions using Agisoft Photoscan v.1.4.3 (<http://www.agisoft.com>),
681 apart from the DEM difference fields displayed in Fig. 4a, which
682 were calculated using the updated Agisoft Metashape 1.5.1. Camera
683 calibration was performed automatically in the bundle adjustment
684 process. From the final dense point clouds, we produced orthophotos
685 at 0.15 m resolution and geoid-corrected DEMs at 0.2 m resolution.
686 Horizontal velocity fields were derived by feature tracking 0.2 m
687 resolution multidirectional hillshade models (produced using GDAL
688 2.2) using OpenPIV feature tracking software (49), using an interro-
689 gation window size of 320x320 pixels and a spacing of 32 pixels (final
690 resolution: 6.4 m). We filtered erroneous values using manually
691 chosen upper and lower thresholds for velocity, signal-to-noise ratio
692 (SNR), and divergence from mean annual flow direction. Uncertain-
693 ties in the velocity field were calculated based on a displacement
694 uncertainty of 0.17 cm, following (48).

695 When calculating uplift from DEM differencing, we assume the
696 vertical uncertainty to be ± 0.2 m following (48), which is close
697 to the scale of uplift explored. However, validation against the
698 observed GPS uplift gives some confidence, with a reported GPS
699 uplift of 0.31 cm between the survey periods comparing with a
700 mean UAV-derived uplift of 0.34 ± 0.05 m across a 6 m² sample
701 area around the GPS location. Survey precision estimates (50) were
702 centimetric, so uncertainty was likely dominated by survey-wide
703 systematic biases, giving confidence to this validation measurement.

704 **Hydrological Routing.** As surface water reaches the ice bed, we as-
705 sume that it flows following gradients in hydraulic potentials. These
706 are calculated using a multiflow direction algorithm, where the flow
707 is diverted to multiple downslope cells in proportion to the slope
708 between them (51, 52). The gradients in hydraulic potential surface
709 are calculated over the catchment of Store Glacier using:

$$\nabla\theta = \rho_w g \nabla Z_b + \alpha \rho_i g \nabla H \quad [1] \quad 710$$

711 with $\nabla\theta$ the gradient of the hydraulic potential surface (Pa), ρ_w
712 and ρ_i the density of water and ice respectively (kg m⁻³), and g the
713 constant of gravitational acceleration (m s⁻²). The glacier geometry
714 is defined with the gradient of bed elevation (∇Z_b , m) and the
715 gradient of ice thickness (∇H , m), taken from BedMachine V3 (53)
716 at 150 m spatial resolution. The coefficient α is a floatation fraction,
717 here set to 1 with the assumption that the subglacial water pressure
718 is equal to the ice overburden pressure. Note that the routing of
719 water in our study region remains similar if we assume that the
720 pressure in the hydrological system is just less than the overburden
721 value ($\alpha = 0.9$).

722 In order to derive discharge from mapped hydraulic potential,
723 we use, as input to the subglacial system, gridded total daily runoff
724 from regional climate model RACMO2. A slightly updated model is
725 used relative to that presented in (54): no model physics have been
726 changed, but the spatial resolution of the model has been increased
727 to 5.5 km from 11 km (although output is downscaled to 1 km).
728 Data for the day of drainage was not available at the time of the
729 study. Instead, we use data for 2017-07-26 (a day where a large
730 rainfall event was observed at the study site) as a proxy for a period
731 when high total water input was entering the subglacial system.
732 Discharge was mapped extending ~140 km inland from the calving
733 front, although only a small section of this is presented in Fig. 4c.

734 **Optical satellite imagery.** Where optical satellite images were down-
735 loaded for RGB visualisation, Sentinel-2 imagery was downloaded
736 from the Copernicus Open Access Hub (scihub.copernicus.eu) and
737 Landsat 8 OLI imagery from the USGS Earth Explorer (earthexplorer.usgs.gov).
738 Long-term lake drainage history for Lake 028, Lake F,
739 and North Lake were produced using imagery visualised with the
740 Google Earth Engine Digitisation Tool (GEEDIT; 55).

741 **Ice Surface Strain Rates.** First and second principal strain rates and
742 directions were calculated from MEaSURES velocity data for 2017
743 (28). We compute the horizontal part of the strain rate tensor,
744 with derivatives approximated by finite difference of the horizontal
745 velocity field (56, 57). The first principal strain rate was calculated

746 as the highest eigenvalue of the strain rate tensor, and the associated
747 eigenvector is the first principal direction. The second principal
748 strain rate (direction) was the lowest eigenvalue (eigenvector).

749 **Data Deposition.** The geophysical time-series, UAV-derived raster,
750 and modelled water routing data reported in this paper are available
751 at the [PROVISIONAL: UK Polar Data Centre], [PROVISIONAL:
752 DOI LINK].

753 **ACKNOWLEDGMENTS.** This research was funded by the Euro-
754 pean Research Council as part of the RESPONDER project under
755 the European Union's Horizon 2020 research and innovation pro-
756 gramme (grant 683043). TRC was supported by a Natural Environ-
757 ment Research Council Doctoral Training Partnership Studentship
758 (grant NE/L002507/1). We are very grateful to Ann Andreassen and
759 the Uummannaq Polar Institute for their kind hospitality, to Rob
760 Law and Sean Peters for their assistance with UAV launches, and
761 to Brice Noël for providing RACMO2 data.

- 762 1. SB Das, et al., Fracture propagation to the base of the Greenland Ice Sheet during
763 supraglacial lake drainage. *Sci.* **320**, 778–781 (2008).
- 764 2. SH Doyle, et al., Ice tectonic deformation during the rapid in situ drainage of a supraglacial
765 lake on the Greenland Ice Sheet. *The Cryosphere* **7**, 129–140 (2013).
- 766 3. LA Stevens, et al., Greenland supraglacial lake drainages triggered by hydrologically induced
767 basal slip. *Nat.* **522**, 73 (2015).
- 768 4. I Bartholomew, et al., Seasonal evolution of subglacial drainage and acceleration in a Green-
769 land outlet glacier. *Nat. Geosci.* **3**, 408 (2010).
- 770 5. AV Sundal, et al., Melt-induced speed-up of Greenland ice sheet offset by efficient subglacial
771 drainage. *Nat.* **469**, 521 (2011).
- 772 6. T Moon, et al., Distinct patterns of seasonal Greenland glacier velocity. *Geophys. research*
773 *letters* **41**, 7209–7216 (2014).
- 774 7. SH Doyle, et al., Persistent flow acceleration within the interior of the Greenland ice sheet.
775 *Geophys. Res. Lett.* **41**, 899–905 (2014).
- 776 8. AJ Tedstone, et al., Decadal slowdown of a land-terminating sector of the Greenland Ice
777 Sheet despite warming. *Nat.* **526**, 692 (2015).
- 778 9. S Sugiyama, A Bauder, M Huss, P Riesen, M Funk, Triggering and drainage mechanisms of the
779 2004 glacier-dammed lake outburst in Gornergletscher, Switzerland. *J. Geophys. Res.*
780 *Earth Surf.* **113** (2008).
- 781 10. CF Dow, et al., Modeling of subglacial hydrological development following rapid supraglacial
782 lake drainage. *J. Geophys. Res. Earth Surf.* **120**, 2014JF003333 (2015).
- 783 11. M Tedesco, et al., Ice dynamic response to two modes of surface lake drainage on the Green-
784 land ice sheet. *Environ. Res. Lett.* **8**, 034007 (2013).
- 785 12. M Hoffman, G Catania, T Neumann, L Andrews, J Rummil, Links between acceleration, melt-
786 ing, and supraglacial lake drainage of the western Greenland Ice Sheet. *J. Geophys. Res.*
787 *Earth Surf.* **116** (2011).
- 788 13. LC Andrews, et al., Seasonal evolution of the subglacial hydrologic system modified by
789 supraglacial lake drainage in Western Greenland. *J. Geophys. Res. Earth Surf.* **123**, 1479–
790 1496 (2018).
- 791 14. MJ Hoffman, et al., Widespread moulin formation during supraglacial lake drainages in Green-
792 land. *Geophys. Res. Lett.* **45**, 778–788 (2018).
- 793 15. G Catania, T Neumann, Persistent englacial drainage features in the Greenland Ice Sheet.
794 *Geophys. Res. Lett.* **37** (2010).
- 795 16. I Howat, S De la Pena, J Van Angelen, J Lenaerts, M Van den Broeke, Brief Communication
796 “Expansion of meltwater lakes on the Greenland ice sheet”. *The Cryosphere* **7**, 201–204
797 (2013).
- 798 17. AAW Fitzpatrick, et al., A decade (2002–2012) of supraglacial lake volume estimates across
799 Russell Glacier, West Greenland. *Cryosphere* **8**, 107–121 (2014).
- 800 18. SW Cooley, P Christoffersen, Observation bias correction reveals more rapidly draining lakes
801 on the Greenland Ice Sheet. *J. Geophys. Res. Earth Surf.* **122**, 1867–1881 (2017).
- 802 19. A Sole, et al., Winter motion mediates dynamic response of the Greenland Ice Sheet to
803 warmer summers. *Geophys. Res. Lett.* **40**, 3940–3944 (2013).
- 804 20. T Meierbachtol, J Harper, N Humphrey, Basal Drainage System Response to Increasing
805 Surface Melt on the Greenland Ice Sheet. *Sci.* **341**, 777–779 (2013).
- 806 21. M Bougamont, et al., Sensitive response of the Greenland Ice Sheet to surface melt drainage
807 over a soft bed. *Nat. Commun.* **5**, 5052 (2014).
- 808 22. N Selmes, T Murray, T James, Characterizing supraglacial lake drainage and freezing on the
809 Greenland Ice Sheet. *The Cryosphere Discuss.* **7**, 475–505 (2013).
- 810 23. B Morriss, et al., A ten-year record of supraglacial lake evolution and rapid drainage in
811 West Greenland using an automated processing algorithm for multispectral imagery. *The*
812 *Cryosphere* **7**, 1869–1877 (2013).
- 813 24. AG Williamson, IC Willis, NS Arnold, AF Banwell, Controls on rapid supraglacial lake drainage
814 in West Greenland: an Exploratory Data Analysis approach. *J. Glaciol.* **64**, 208–226 (2018).
- 815 25. P Christoffersen, et al., Cascading lake drainage on the Greenland Ice Sheet triggered by
816 tensile shock and fracture. *Nat. communications* **9**, 1064 (2018).
- 817 26. JD Carmichael, et al., Seismicity on the western Greenland Ice Sheet: Surface fracture in the
818 vicinity of active moulins. *J. Geophys. Res. Earth Surf.* **120**, 1082–1106 (2015).
- 819 27. PW Nienow, AJ Sole, DA Slater, TR Cowton, Recent Advances in Our Understanding of
820 the Role of Meltwater in the Greenland Ice Sheet System. *Curr. Clim. Chang. Reports* **3**,
821 330–344 (2017).
- 822 28. I Joughin, BE Smith, IM Howat, T Scambos, T Moon, Greenland flow variability from ice-
823 sheet-wide velocity mapping. *J. Glaciol.* **56**, 415–430 (2010).
- 824 29. C Porter, et al., ArcticDEM (2018).
30. RB Alley, TK Dupont, BR Parizek, S Anandakrishnan, Access of surface meltwater to beds of
825 sub-freezing glaciers: preliminary insights. *Annals Glaciol.* **40**, 8–14 (2005).
- 826 31. K Lindbäck, et al., Subglacial water drainage, storage, and piracy beneath the Greenland ice
827 sheet. *Geophys. Res. Lett.* **42**, 7606–7614 (2015).
- 828 32. SJ Livingstone, et al., Brief communication: Outburst floods triggered by periodic drainage
829 of subglacial lakes, isunguata sermia, west greenland. *The Cryosphere Discuss.* **2019**, 1–8
830 (2019).
- 831 33. I Joughin, et al., Influence of ice-sheet geometry and supraglacial lakes on seasonal ice-flow
832 variability. *The Cryosphere* **7**, 1185–1192 (2013).
- 833 34. N Selmes, T Murray, T James, Fast draining lakes on the Greenland Ice Sheet. *Geophys.*
834 *Res. Lett.* **38** (2011).
- 835 35. AG Williamson, NS Arnold, AF Banwell, IC Willis, A Fully Automated Supraglacial lake area
836 and volume Tracking (“FAST”) algorithm: Development and application using MODIS imagery
837 of West Greenland. *Remote. Sens. Environ.* **196**, 113–133 (2017).
- 838 36. AG Williamson, AF Banwell, IC Willis, NS Arnold, Dual-satellite (Sentinel-2 and Landsat 8)
839 remote sensing of supraglacial lakes in Greenland. *The Cryosphere* **12**, 3045–3065 (2018).
- 840 37. CC Clason, et al., Modelling the transfer of supraglacial meltwater to the bed of Leverett
841 Glacier, Southwest Greenland. *The Cryosphere* **9**, 123–138 (2015).
- 842 38. C Koziol, N Arnold, A Pope, W Colgan, Quantifying supraglacial meltwater pathways in the
843 Paakitsoq region, west Greenland. *J. Glaciol.* **63**, 464–476 (2017).
- 844 39. D McGrath, W Colgan, K Steffen, P Lauffenburger, J Balog, Assessing the summer water
845 budget of a moulin basin in the Sermeq Avannarleq ablation region, Greenland ice sheet. *J.*
846 *Glaciol.* **57**, 954–964 (2011).
- 847 40. C Schoof, Ice-sheet acceleration driven by melt supply variability. *Nat.* **468**, 803 (2010).
- 848 41. K Poinar, et al., Limits to future expansion of surface-melt-enhanced ice flow into the interior
849 of western Greenland. *Geophys. Res. Lett.* **42**, 1800–1807 (2015).
- 850 42. J Mougnot, et al., Forty-six years of Greenland Ice Sheet mass balance from 1972 to 2018.
851 *Proc. Natl. Acad. Sci.* **116**, 9239–9244 (2019).
- 852 43. Copernicus Climate Change Service, ERA5: Fifth generation of ECMWF atmospheric reanal-
853 yses of the global climate (Copernicus Climate Change Service Climate Data Store (CDS)
854 (<https://cds.climate.copernicus.eu/cdsapp#!/home>) (2017) Accessed: 2019-01-19).
- 855 44. M King, Rigorous GPS data-processing strategies for glaciological applications. *J. Glaciol.*
856 **50**, 601–607 (2004).
- 857 45. G Chen, Ph.D. thesis (Massachusetts Institute of Technology) (1998).
- 858 46. JM Dow, RE Neilan, C Rizo, The international GNSS service in a changing landscape of
859 global navigation satellite systems. *J. Geod.* **83**, 191–198 (2009).
- 860 47. SH Doyle, Ph.D. thesis (Aberystwyth University) (2014).
- 861 48. TR Chudley, P Christoffersen, SH Doyle, A Abellan, N Snooke, High-accuracy UAV pho-
862 togrammetry of ice sheet dynamics with no ground control. *The Cryosphere* **13**, 955–968
863 (2019).
- 864 49. ZJ Taylor, R Gurka, GA Kopp, A Liberzon, Long-duration time-resolved PIV to study unsteady
865 aerodynamics. *IEEE Transactions on Instrumentation Meas.* **59**, 3262–3269 (2010).
- 866 50. MR James, S Robson, MW Smith, 3-D uncertainty-based topographic change detection with
867 structure-from-motion photogrammetry: precision maps for ground control and directly geo-
868 referenced surveys. *Earth Surf. Process. Landforms* **42**, 1769–1788 (2017).
- 869 51. TG Freeman, Calculating catchment area with divergent flow based on a regular grid. *Com-
870 put. & Geosci.* **17**, 413–422 (1991).
- 871 52. P Quinn, K Beven, P Chevallier, O Planchon, The prediction of hillslope flow paths for dis-
872 tributed hydrological modelling using digital terrain models. *Hydrol. processes* **5**, 59–79
873 (1991).
- 874 53. M Morigthem, et al., BedMachine v3: Complete bed topography and ocean bathymetry map-
875 ping of Greenland from multibeam echo sounding combined with mass conservation. *Geo-
876 phys. Res. Lett.* **44**, 11–051 (2017).
- 877 54. B Noël, et al., Modelling the climate and surface mass balance of polar ice sheets using
878 RACMO2 – Part 1: Greenland (1958–2016). *Cryosphere* **12**, 811–831 (2018).
- 879 55. JM Lea, The Google Earth Engine Digitisation Tool (GEEDiT) and the Margin change Quan-
880 tification tool (MaQIT)—simple tools for the rapid mapping and quantification of changing Earth
881 surface margins. *Earth Surf. Dyn.* **6**, 551–561 (2018).
- 882 56. G Jouvét, et al., Initiation of a major calving event on the Bowdoin Glacier captured by UAV
883 photogrammetry. *The Cryosphere* **11**, 911–921 (2017).
- 884 57. KE Alley, et al., Continent-wide estimates of Antarctic strain rates from Landsat 8-derived
885 velocity grids. *J. Glaciol.* **64**, 321–332 (2018).
- 886